Orbit Simulator for Satellite and Near-Space Platforms Supporting Observing System Simulation Experiments

LIKUN WANG,[a,b] NARGES SHAHROUDI,[b,c] ERIC MADDY,[b,c] KEVIN GARRETT,[b] SID BOUKABARA,[b] ROSS HOFFMAN,[a,b] AND KAYO IDE[d]

[a] *Cooperative Institute for Satellite Earth System Studies, Earth System Science Interdisciplinary Center, University of Maryland, College Park, College Park, Maryland*
[b] *NOAA/NESDIS/Center for Satellite Applications and Research, College Park, Maryland*
[c] *Riverside Technology, Inc., Fort Collins, Colorado*
[d] *Department of Atmospheric and Oceanic Science, University of Maryland, College Park, College Park, Maryland*

ABSTRACT: Developed at the National Oceanic and Atmospheric Administration (NOAA) and the Joint Center for Satellite Data Assimilation (JCSDA), the Community Global Observing System Simulation Experiment (OSSE) Package (CGOP) provides a vehicle to quantitatively evaluate the impacts of emerging environmental observing systems or emerging in situ or remote sensing instruments on NOAA numerical weather prediction (NWP) forecast skill. The typical first step for the OSSE is to simulate observations from the so-called nature run. Therefore, the observation spatial, temporal, and view geometry are needed to extract the atmospheric and surface variables from the nature run, which are then input to the observation forward operator (e.g., radiative transfer models) to simulate the new observations. This is a challenge for newly proposed systems for which instruments are not yet built or platforms are not yet deployed. To address this need, this study introduces an orbit simulator to compute these parameters based on the specific hosting platform and onboard instrument characteristics, which has been recently developed by the NOAA Center for Satellite Applications and Research (STAR) and added to the GCOP framework. In addition to simulating existing polar-orbiting and geostationary orbits, it is also applicable to emerging near-space platforms (e.g., stratospheric balloons), cube satellite constellations, and Tundra orbits. The observation geometry simulator includes not only passive microwave and infrared sounders but also global navigation satellite system/radio occultation (GNSS/RO) instruments. For passive atmospheric sounders, it calculates the geometric parameters of proposed instruments on different platforms, such as time varying location (latitude and longitude), scan geometry (satellite zenith and azimuth angles), and ground instantaneous field of view (GIFOV) parameters for either cross-track or conical scanning mechanisms. For RO observations, it determines the geometry of the transmitters and receivers either on satellites or stratospheric balloons and computes their slant paths. The simulator has been successfully applied for recent OSSE studies (e.g., evaluating the impacts of future geostationary hyperspectral infrared sounders and RO observations from stratospheric balloons).

SIGNIFICANCE STATEMENT: An orbit simulator for satellite and near-space platforms for supporting observing system simulation experiments (OSSE) is developed in this study. It can compute spatial, temporal, and view geometry parameters of the new observations based on the specific hosting platform and onboard instrument characteristics. These parameters are important for the OSSE to extract atmospheric profiles and surface properties from nature run data and simulate new observations. In addition to simulating existing polar-orbiting and geostationary orbits, it is applicable to emerging near-space platforms (e.g., stratospheric balloons), cube satellite constellations, and Tundra orbits. The observation geometry simulator includes not only passive microwave and infrared sounders but also radio occultation instruments.

KEYWORDS: Instrumentation/sensors; Measurements; Remote sensing; Satellite observations

1. Introduction

The Community Global Observing System Simulation Experiments (OSSE) Package (CGOP) was developed at the National Oceanic and Atmospheric Administration and Joint Center for Satellite Data Assimilation (JCSDA) for conducting OSSE studies (Boukabara et al. 2016, 2018a, b). In an OSSE, observations simulated from the nature run (NR)—usually a long free-running numerical weather prediction (NWP) forecast (e.g., Putman et al. 2014)—are assimilated in a data assimilation and forecast system to evaluate impacts

from different designs of new satellite systems before their instruments are built or deployed, and to compare the performance of new systems against current observing systems. The results can help to guide the design of new instruments and to determine whether a new satellite system is cost-effective (Hoffman and Atlas 2016). As the first step, the GCOP must simulate new observations from proposed observational systems. This requires the time and location of individual observations and their observing geometry to extract the coincident atmospheric and surface variables from the nature run, which are then input to the observation forward operator (e.g., radiative transfer model and radio occultation forward operator). Relying on existing observing systems or those having similar

characteristics, the current CGOP practice is to extract the time, location, and geometry parameters taken from the radiance diagnostics files that were created and archived from the operational data assimilation at the NOAA National Centers for Environmental Prediction (NCEP). This is applicable for currently existing observing systems, such as the Constellation Observing System for Meteorology, Ionosphere and Climate (COSMIC)-2 or the sensors of the Joint Polar Satellite System (JPSS) and Geostationary Operational Environmental Satellite (GOES) series. However, for newly proposed systems without related geometry or orbital characteristics available from legacy platforms and instruments, an orbit simulator is needed to compute the parameters based on the new specifications. For example, with emerging cube or small satellite technology, it is possible to launch a group of satellites with similar instruments in the same or similar orbital plane. Given the successful operation of Loon platforms for internet access to rural and remote areas, the use of high-altitude balloons, as demonstrated by organizations such as Loon (Candido 2020), could be platforms leveraged for remote sensing instruments and compliment the current global observing system (GOS). In addition, NOAA is currently assessing configurations of the next-generation space architecture, including the potential impacts of a constellation of geostationary hyperspectral sounders on global medium-range forecasts through OSSEs (Casey et al. 2018; Li et al. 2018; Wang et al. 2021) as well as to evaluate the benefits of Tundra orbit platforms for polar region coverage (Li et al. 2021). How these future systems can benefit the GOS, and further impact NOAA NWP forecasting capability must be quantitatively and rapidly assessed using the OSSE capabilities.

To address the critical need to conduct OSSE experiments for new observing systems, an orbit simulator has been recently developed within the GCOP. In addition to simulating existing polar-orbiting and geostationary orbits, it is also applicable to emerging near-space platforms (e.g., stratospheric balloons), CubeSat constellations, and Tundra orbits. The instrument geometry simulator includes not only passive microwave (MW) and infrared (IR) sounders but also radio occultation (RO) instruments. For passive atmospheric sounders, it can calculate the geometric parameters of proposed instruments on different platforms, such as time varying location (latitude and longitude), scan geometry (satellite zenith and azimuth angles), and ground instantaneous field of view (GIFOV) parameters. For the RO instruments, it determines the geometry between the global navigation satellite system (GNSS) transmitters and the receivers on satellites or stratospheric balloons and computes the slant path of the GNSS RO observations. Figure 1 depicts the processes within the orbit simulator. First, the hosting platform's flight through the nature run is determined by the known orbit parameters or the known trajectories. Second, the specified payload sensor's scan mechanisms determine its view of Earth's atmosphere and surface. These two steps together generate the sensor geometry parameters for the CGOP to simulate the observations. Accordingly, the CGOP is composed of four parts, including 1) flight platform simulator, 2) instrument geometry simulator, 3) observation simulator, and 4) observation impact experiments. Parts 3 and 4 have been discussed in the

previous GCOP studies (Boukabara et al. 2016, 2018a, 2018b). Here we describe and validate the new platform and instrument geometry simulator.

The paper is organized as follows: Section 2 describes the orbit simulator for space (satellite) and near-space (stratospheric balloons) platforms, respectively. Section 3 presents the instrument simulator including passive atmospheric sounders and RO systems, and instruments. Section 4 presents a summary, caveats, and future planned extensions of the CGOP orbit determination and sensor geometry simulation.

2. Platform simulator

The flight platform simulator must compute how a payload hosting platform moves in three-dimensional space (longitude, latitude, and altitude) with time relative to the Earth ellipsoid. In this study, the World Geodetic System 1984 (WGS84) is used as a geodetic reference (datum) to characterize the Earth ellipsoid. This section focuses on satellite and high-altitude balloon platforms. Additional human controlled platforms that can also host instruments include platforms such as aircraft, unmanned aerial vehicles, ocean-subsurface autonomous vehicles. Aircraft and ships are often navigated to take advantage of winds and currents. On the other hand, aircraft are also constrained to limit crew exposure to radiation and thus take less efficient but safer routes. For OSSE experiments, we can add any known designed or specified travel paths of these platforms.

a. Satellite platform simulator

For an Earth observing satellite used for OSSE studies, we consider three types of satellite orbits according to altitude, 1) low-Earth orbits (LEO) with altitudes below 1000 km, 2) a geostationary orbit (GEO) with an altitude of 35 786 km, and 3) a Tundra orbit that is highly elliptical orbit with apogee above 35 786 km. A geostationary satellite stays in a fixed longitude position on the Earth equator with an altitude of 35 786 km and is assumed to be static with time. This section will focus on the simulator developed for LEO and Tundra orbiting platforms, while section 3 will illustrate an example of a hyperspectral geostationary sounder.

To simulate a satellite orbit, the most common approach is to use the Simplified Perturbations model 4 (SPG4) to calculate the six-component time-varying orbital state vector of a satellite (position and velocity) relative to the Earth-centered inertial (ECI) coordinate system. (The coordinate systems used in this study are summarized in Table 1.) The SGP4 model was developed by North American Aerospace Defense Command (NORAD) Air Force Space Command (AFSPC) for the space catalogue use in the 1970s (Vallado et al. 2006). The model predicts the effects of perturbations caused by Earth's shape, drag, radiation, and gravitation effects from other bodies such as the sun and moon using the two-line elements (TLE) as inputs. A TLE file is a data format encoding a list of orbital elements of an Earth-orbiting object for a given point in time, the epoch, including 1) inclination, 2) right ascension of the ascending node, 3) eccentricity argument of perigee, 4) mean anomaly, and 5) mean motion (revolutions per day). The TLE datasets are
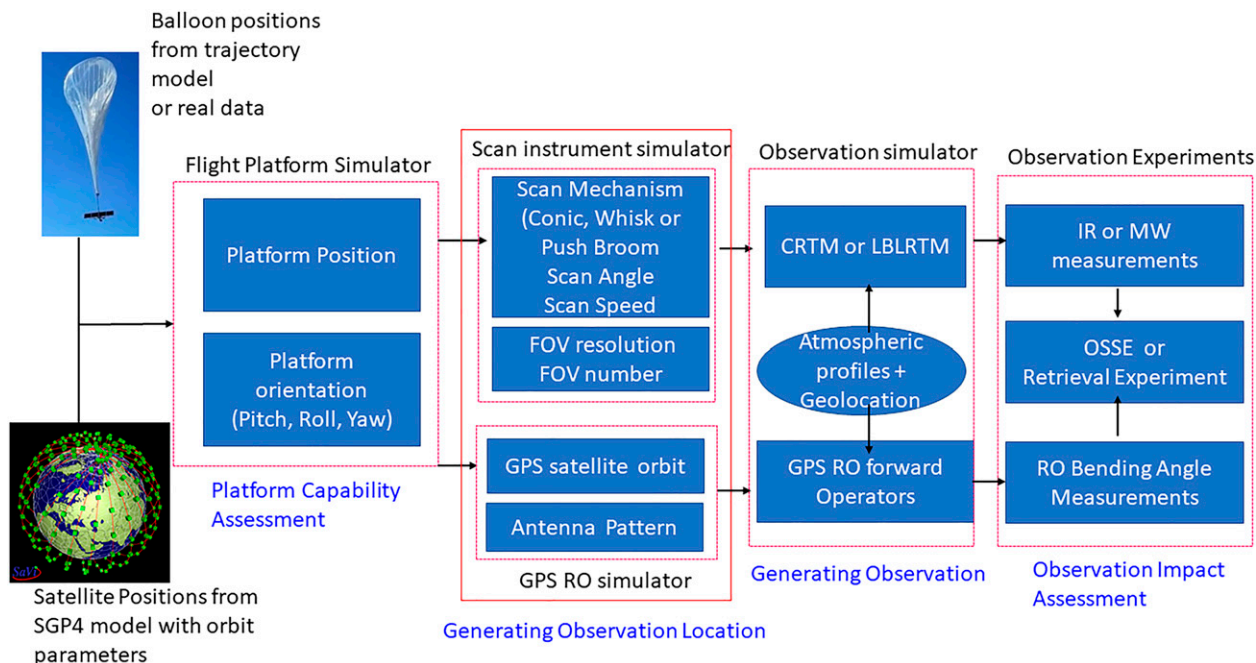
FIG. 1. Flowchart of the satellite and near-space platform simulator.

now distributed by http://www.celestrak.com/ and by http://www.space-track.org/. For a typical OSSE experiment using the CGOP, the satellites are assumed to fly in the nature run model fields; therefore, our strategy is to use or modify available TLE files for the existing or similar satellite orbits (the detailed explanation of TLE file format can be found at https://www.space-track.org/documentation#/tle). For the proposed satellites that are not launched yet, the new TLE file is generated based on the proposed orbit information.

Finally, the SGP4 model outputs orbital state vectors including satellite position and speed in the ECI coordinate system. We use the Naval Observatory Vector Astrometry Software (NOVAS) version 3.1 by doing rotations for wobble (polar wander), spin (Earth rotation), nutation, and precession to transform the vectors from ECI to the Earth-centered, Earth-fixed (ECEF) coordinate system (Barron et al. 2011); the vector in ECEF are then converted into latitude, longitude, and altitude.

A typical LEO orbit example, demonstrated in Fig. 2a, is the launch of the first 60 SpaceX Starlink internet satellite constellation positioned at 0008 UTC 9 June 2019 predicted by the SGP4 model with a 53.0° inclination at a 450-km orbit. The attached animation file gives the details on how these satellites move. Figure 2b shows the planned Starlink phase one constellation, with 24 orbits each populated by 66 satellites. The final purpose of Starlink is to provide broadband internet service coverage continuously at any place on Earth. In addition, there is ongoing research to explore how small satellite constellations can add value to NOAA as part of the next-generation environmental satellite architecture (the corresponding study can be found from the website of the NOAA Systems performance Assessment Team at https://www.star.nesdis.noaa.gov/sat/index.php).

Traditionally, NOAA satellites are either on LEO or GEO. LEO satellites are constantly moving around Earth with global revisit times ranging from hours to days, while GEO satellites have high temporal resolution for monitoring environmental conditions but are limited to tropical and extratropical regions not including the polar regions. Thus, there are coverage gaps at high latitudes. A satellite on a highly elliptical, high inclination, geosynchronous orbit, known as a Tundra orbit, hovers most of the day due to apogee dwell above one of the polar regions and can fill this gap (Trishchenko et al. 2016). Figure 3 presents an example of such a Tundra orbit, with an inclination 63.4°, perigee at 24 473.9909 km and 63.6°S latitude and apogee at 47 133.8319 km and 63.6°N latitude. As seen in the spacing of the location fixes in Fig. 3, the satellite travels very slowly, or dwells, at apogee. Specifically, a Tundra platform dwells for almost eight hours traveling around the small circle above 50°N. To be geosynchronous, the Tundra orbital period is one sidereal day, i.e., four minutes shorter than a solar day.

Finally, in order to quantitatively validate the satellite platform simulator, we randomly choose one orbit of Cross-Track Infrared Sounder (CrIS) data from the *Suomi National Polar-Orbiting Partnership* (*SNPP*) from 0822 to 1022 UTC 29 January 2017. Its brightness temperature (BT) image at 900.00 cm^{-1} (11.1 μm) is given in Fig. 4a. Specifically, the dataset contains the actual satellite position and velocity vectors in ECEF at each scan, which were derived from the real-time global positioning system (GPS) data from an onboard GPS receiver. On the other hand, we use the TLE file dated on the same day as the input to predict the orbit vectors in ECEF for the same scan time. For straightforward comparison, the satellite position vectors both from the data and simulator are

TABLE 1. Summary of the coordinate systems used in this study.

Coordinate systems	Type	Origin	Axes conventions	Variables
Geodetic latitude, longitude, and altitude (LLA) coordinate	Spherical	Earth center	Latitude is an angle that ranges from 0° at the equator to 90° (north or south) at the poles; positive longitudes are east of the prime meridian, and negative ones are west	(φ, λ, h) φ: Geodetic latitude (°) λ: Longitude (°) h: Altitude (m)
Local spherical coordinate	Spherical	Measurement location	The range is the Euclidean distance from the origin to the target, the zenith angle is the angle between the zenith direction and the line from the origin to the target, the azimuth angle is the signed angle measured from the azimuth reference direction to the orthogonal projection of the line segment from the origin to the target on the reference plane	(R, Θ, Φ) R: Range (m) Θ: Zenith angle (°) Φ: Azimuth angle (°)
Local east, north, up (ENU) coordinate	Cartesian	Measurement location	East–west tangent to parallels, north–south tangent to meridians, and, up–down in the direction normal to the oblate spheroid used as Earth's ellipsoid	(East, north, up) in meters
Earth-centered, Earth-fixed (ECEF) coordinate	Cartesian	Earth center	The z axis coincides with the minor axis of the reference ellipsoid. The x axis runs from the origin through a point on the equatorial plane at the zero meridian; the y axis is perpendicular to the x axis on the equatorial plane	(x, y, z) in meters
Earth-centered inertial (ECI) coordinate	Cartesian	Earth center	Same as ECEF, but the x axis and y axis do not rotate with the Earth ellipsoid	(x, y, z) in meters
Orbital (or trajectory) coordinate system (OCS) coordinate	Cartesian	Spacecraft center of mass	The z axis points to nadir, the x axis points to the platform instantaneous moving direction, and the y axis is the normalized cross product of the z axis and x axis	(x, y, z) in meters
GEO fixed grid frame	Spherical	The ideal subsatellite point	The z axis points to nadir, the y axis points south, and the x axis points east	(θ, φ) in degrees θ: EW angle (°) φ: SN angle (°)
Spacecraft body frame (SBF) coordinate	Cartesian	Spacecraft center of mass	Perfectly align with OCS, if pitch, roll, and yaw are zeros	(x, y, z) in meters

converted into nadir longitudes and latitudes. Their great-circle distances on the Earth surface are calculated and shown in Fig. 4b. It indicates that the errors from the simulator are less than 0.6 km in a whole orbit compared to actual nadir locations. This suggests that the orbit simulator performs well once the orbit parameters are provided. If the orbit parameters are not updated often, the error will grow approximately 1–3 km per day and accumulate (Vallado et al. 2006).

b. Near-space platform

Stratosphere balloons are another new potential platform to host remote sensing instruments. Such systems can also be quantitatively assessed with OSSEs. For example, Loon LLC—an Alphabet Inc. subsidiary—uses high-altitude balloons placed in the stratosphere to provide internet access to rural and remote areas. Typically drifting with stratospheric
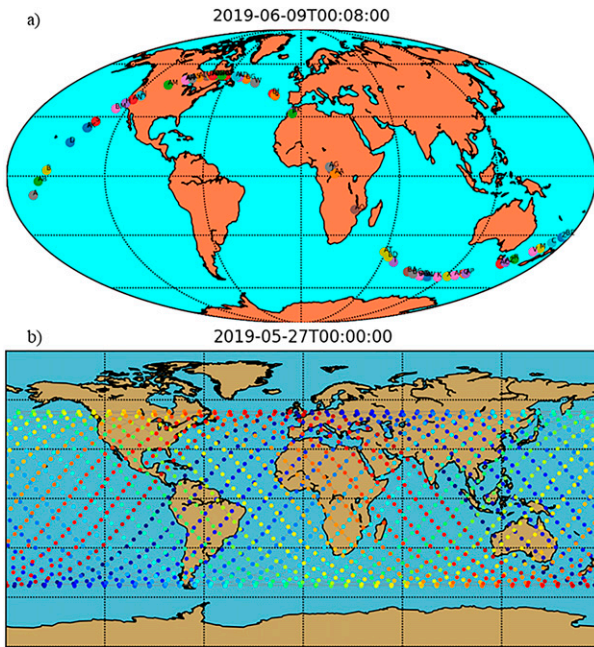
FIG. 2. (a) The first launch of 60 Space-X Starlink test satellite constellation at 0008 UTC 9 Jun 2019 simulated by the SGP4 model. (b) The planned Starlink phase one constellation including 24 orbits, and each orbit has 66 satellites. The dots in the figures indicate the instantaneous nadir location of the satellites.
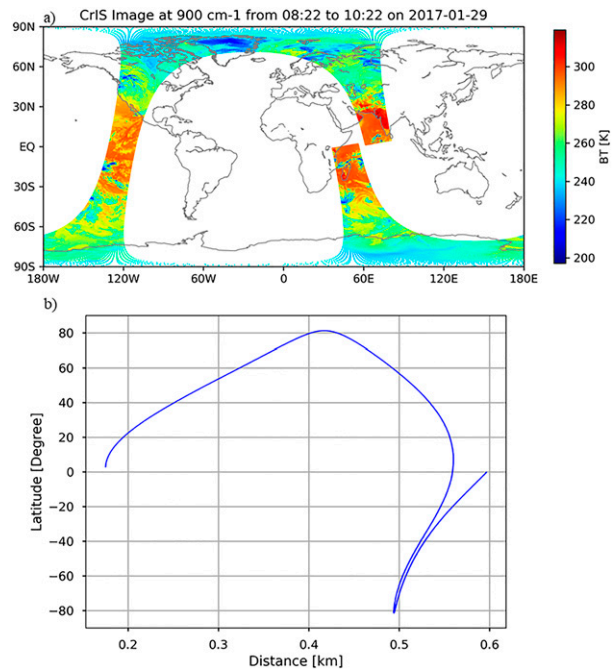

FIG. 4. (a) *SNPP* CrIS BT images at 900 cm^{-1} from 0822 to 1022 UTC 29 Jan 2017 and (b) the great-circle distance of the satellite nadir locations from the real data and those predicted from the orbit simulator.

winds near 20 km in altitude (30–50 hPa), the balloons can be moved to higher or lower altitudes to control the direction of motion and remain aloft continuously for weeks to months. These balloons provide in situ measurements of ambient air

FIG. 3. Ground track of a Tundra orbit for one day. Because of apogee dwell (the satellite slows down at apogee), it spends most of its time over a high latitude area. The points are plotted every 10 min.

temperature, air pressure, and wind velocity (derived from GNSS locations), along with an Earth-view, single window channel IR radiation flux (Candido 2020). The stratosphere balloons can potentially serve as high-altitude "pseudo-satellite" platforms to host instruments (e.g., RO receivers). It is for this reason that the near-space platform simulator is included in the package.

Stratosphere balloons are a type of superpressure balloon filled with helium. Following the approach by Riddle et al. (2006), we developed a simple trajectory model to predict the flight path of a high-altitude balloon using the horizontal atmospheric motion, i.e., the wind field from the GEOS-5 Nature Run (G5NR; Putman et al. 2014). Specifically, assuming an ideal, infinitely small air parcel, the trajectory of the balloon is governed by the differential trajectory equation:

$$\frac{d\mathbf{X}}{dt} = \mathbf{V}(\mathbf{X}, \, t), \tag{1}$$

where $\mathbf{X} = (x, y, z)$ denotes the position of the air parcel and $\mathbf{V} = (u, v, \omega)$ is the vector velocity. Vertically, a superpressure balloon generally maintains a stable altitude for long periods. The reason is that the volume of a superpressure balloon remains relatively constant in the face of changes in ambient pressure outside the balloon, and changes in the temperature of the helium within the balloon (Levanon et al. 1974; Hertzog et al. 2007). The balloon oscillates around its stable altitude by the vertical motion of the air, which is not considered in the trajectory model. In other words, when the balloon is advected by the nature run horizontal wind field, it is assumed to vertically stay on constant-
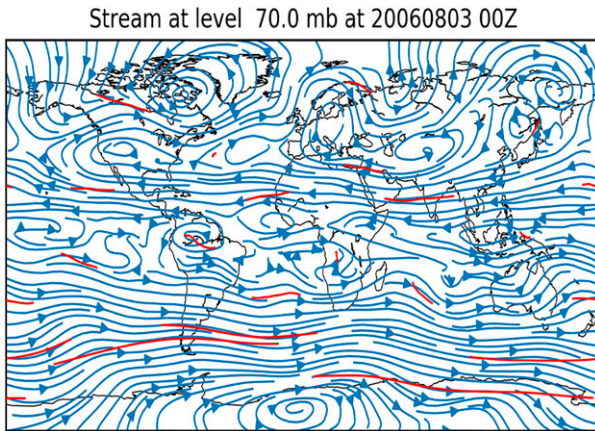
FIG. 5. Twenty superpressure balloons trajectories (red) simulated using the G5NR data. The balloons are flying in the G5NR wind fields for 48 h. The blue lines are an instantaneous snapshot of the streamfunction at 70 hPa at 0000 UTC 3 Aug 2016. The trajectory model began at 0000 UTC 1 Aug 2016 and was integrated with a time step of 0.5 h.

density (isopycnic) surfaces. Therefore, the model assigns a new altitude at a new location for the balloon by searching the same air density value for each integration step. Moreover, in real operations, the balloon occasionally adjusts its altitude by pumping air between the balloon and an internal bladder. This modifies the balloon density and therefore its elevation. Vertical balloon maneuvers are not considered in the trajectory model.

The analytic solution of the above trajectory equation is expressed as

$$\mathbf{X}_1 = \mathbf{X}_0 + \int_{t_0}^{t_1} \mathbf{V}(X_t, t) \, dt \qquad (2)$$

with initial position $\mathbf{X}_0$ at start time t_0 and end time t_1. Different explicit Runge–Kutta numerical integration schemes can be used to solve (2) and thus to compute the trajectory, as has been comprehensively studied by Rößler et al. (2018). In this study, we use the simplest solution of (2)—the first-order Runge–Kutta or explicit Euler method, which is given by

$$X_{n+1} = X_n + \Delta t V(X_n, t_n). \qquad (3)$$

In Eq. (3), $\Delta t = t_{n+1} - t_n$ refers to the time step, which is 30 min for G5NR data. The Euler method is the first-order Runge–Kutta method, which is also referred to as the "zero acceleration" scheme. Given a start point X_n, initial bearing (wind direction), and travel distance, one can calculate the destination point along a (shortest distance) great-circle arc in the NR space using spherical coordinate transformation. Figure 5 gives an example of simulated trajectories for 20 superpressure balloons initially evenly distributed at 19.5 km. The figure clearly shows that the balloons move following the G5NR stratospheric streamflow. The accuracy of computed trajectories is impacted by many factors including the integration schemes (e.g., Rößler et al. 2018), the uncertainties of wind measurements (e.g., Riddle et al. 2006), and the model
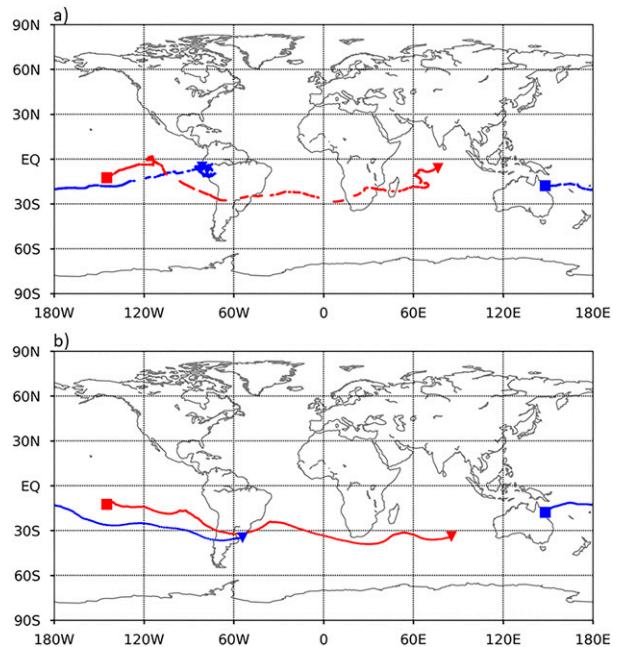

FIG. 6. (a) The trajectories of two stratospheric balloons from Loon LLC traveling in August 2019 and (b) the trajectories calculated by the trajectory model using the G5NR data in August 2006. The trajectories are from the same initial locations. The squares indicate the balloon initial positions while the triangles represent the final position after one month.

forecast time (Stunder 1996). As a qualitative assessment, Fig. 6 compares the trajectories from the two real superpressure balloons launched in August 2019 (Friedrich et al. 2017; Candido 2020) and those computed from the trajectory model using the G5NR data in August 2006. The exact locations of the trajectories are quite different mainly because of the different wind fields. The simulations use wind data from G5NR in 2006 but the Loon trajectory occurred in 2019.

De la Cámara et al. (2010) computed the balloon trajectories using different reanalysis data and the comparison with the real trajectories indicates the similar error structures. However, the balloons traveled in the Southern Hemisphere along similar paths and have comparable coverage, even if they were in different space (G5NR model space versus real data) and in different periods (2006 versus 2019). Therefore, it is good enough to evaluate the impacts of the balloon-based instruments using the calculated trajectories for the OSSE purpose.

c. Platform orientation

For realistic sensor simulations, a module to determine platform orientation is also developed, which is then combined with the computed platform orbit (or trajectory). The platform attitude provides information about a platform's orientation with respect to the platform orbit or trajectory. The three critical flight dynamical attitude parameters are the angles of rotation in three dimensions about the platform's center of gravity, known as pitch, roll, and yaw. The
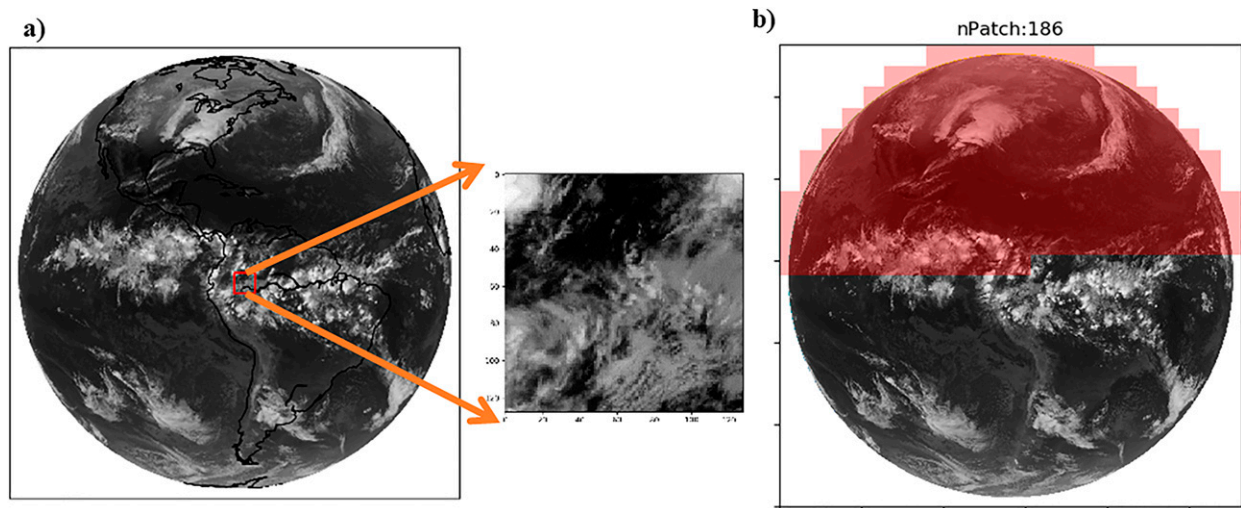
FIG. 7. (a) A large area focal plane array composed of 128×128 pixels, in which each pixel has a corresponding spatial resolution of 4.0 km at nadir. (b) The simulated sounder scan mechanism, which scans Earth via two orthogonal scan mirrors: one east–west (EW) and one north–south (NS).

transformation from the attitude parameters in the spacecraft body frame (SBF) coordinate (see Table 1) to the platform orientation in the orbital (or trajectory) coordinate is a three-dimensional rotation matrix with the components of the rotation matrix being functions of the platform roll, pitch, and yaw attitude angles. The nature of the functions of roll, pitch, and yaw depends on the exact definition of these angles (i.e., how they are generated by the attitude control system). In the simulator, we follow the NOAA satellite attitude definition convention, which follows the order of yaw, roll, and pitch (called type 3-1-2). The equation of the transformation matrix using the three angles can be found in appendix B of JPSS Visible Infrared Imaging Radiometer Suite Geolocation algorithm theoretical basis document (ATBD) (Baker 2011). The transformation matrix is thus determined once the platform attitude parameters are available. Additionally, this allows simulation testing of the impact of attitude stability on the measurements by adding noise to the attitude angles.

3. Instrument geometry simulator

The instrument geometry simulator currently can handle two different types of observing systems: 1) passive atmospheric sounders and 2) RO transmitters and receivers. We focus on these two types since they are the main inputs for NWP data assimilation and the top candidates for proposed CubeSat/SmallSat missions. Passive atmospheric sounders detect the emitted and reflected radiation from the atmosphere and Earth in the infrared and microwave spectral range. Visible and ultraviolet–visible instruments have not been considered in this package because their measurements have not been directly assimilated by the NWP models. The instrument geometry simulations for passive atmospheric sounders are to use the specified instrument scan mechanism (such as scan type—conical or cross-track scanning, scan

range, and scan speed) to add GIFOV (or pixel) parameters so that when the hosting platform flies in space, the simulation software produces observation geometry datasets that include longitude, latitude, view zenith and azimuth angles, solar zenith and azimuth angles, and GIFOV shapes (if needed). Since passive atmospheric sounders have different scan mechanisms on GEO and LEO satellites, these two cases are discussed separately. Following that we discuss the RO observation geometry simulation.

a. Geostationary IR sounder

Geostationary hyperspectral sounders can provide high temporal and high spatial resolution, allowing the production of four-dimensional moisture and dynamic motion information. Such observations would be critical for storm prediction when assimilated into regional- or storm-scale NWP models over conterminous United States (CONUS) (Schmit et al. 2009). The scan mechanism of the Geosynchronous Imaging Fourier Transform Spectrometer is used here to simulate geostationary sounder geometry dataset (Bingham et al. 2006). Specifically, in order to enable frequent high spatial resolution coverage over the full disk of Earth, a large area focal plane array composed of 128×128 pixels is used, in which each pixel has a corresponding spatial resolution of 4.0 km at nadir corresponding to an angular field of view (FOV) of 112 microradians. As shown in Fig. 7, the simulated sounder scans Earth via two orthogonal scan mirrors: one east–west (EW) and one north–south (NS). It first scans in an EW direction and is then stepped to a new NS scan angle to begin another EW swath. In this manner, if the focal plane dwells for 4.7 s for each patch, a total of 392 patches achieve a full disk scan in 30 min. Based on this configuration, the angles of each pixel in the EW and NS direction for every step form the fixed grid frame (FGF) coordinate system (see the definition in Table 1). The line of sight vector (LOS) is parameterized by these two
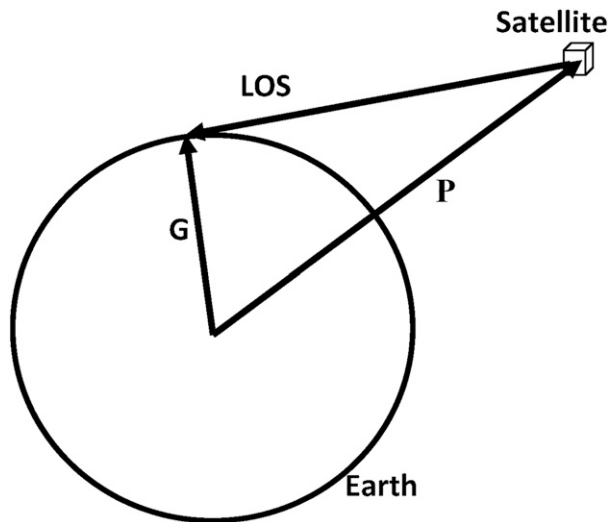
FIG. 8. Schematic diagrams showing the relationship between the LOS vector **LOS**, satellite position vector **P**, and the measurement location vector **G**.

angles—the north/south angle (vertical scan) and east/west angle (horizontal scan). The GOES-R Data Book (NOAA 2018) provides the details on how to convert these two angles into latitude and longitude. Once the longitude and latitude for each pixel is computed, three vectors can be computed using ECEF coordinates, as shown in Fig. 8. The satellite position vector **P** points to the satellite from Earth's center—the ECEF origin, which can be calculated using the longitude and latitude of subsatellite point and satellite altitude. The satellite measurement location vector **G** points to the location of satellite measurements from the Earth center. The satellite LOS vector **LOS** points to the satellite measurement location on the Earth ellipsoid surface from the satellite position. From the figure it is clear that

$$\mathbf{LOS} = \mathbf{G} - \mathbf{P}. \tag{4}$$

This LOS vector in (x, y, z) in ECEF can be converted to the local east, north, up (ENU) coordinate system as (see Fig. 4 in Wang et al. 2016b)

$$\begin{bmatrix} E \\ N \\ U \end{bmatrix} = \begin{pmatrix} -\sin\lambda & \cos\lambda & 0 \\ \cos\lambda\sin\varphi & -\sin\lambda\cos\varphi & \cos\varphi \\ \cos\lambda\cos\varphi & \sin\lambda\cos\varphi & \sin\varphi \end{pmatrix} \begin{bmatrix} x \\ y \\ x \end{bmatrix}, \tag{5}$$

where λ is longitude and φ is latitude at the measurement location. Furthermore, the LOS vector in ENU can be converted to range, zenith angle, and azimuth angle (R, Θ, Φ) in the local spherical coordinate as

$$\begin{bmatrix} R \\ \Theta \\ \Phi \end{bmatrix} = \begin{bmatrix} \sqrt{x^2 + y^2 + z^2} \\ \arccos(U/R) \\ \arctan(E/N) \end{bmatrix}. \tag{6}$$

Figure 9 shows the zenith angle map for a geostationary sounder calculated using the above method. The spatial resolution map is also given in Fig. 9. It clearly shows that the 4.0-km nadir pixel gradually increases to 8–10 km at the scan edge. This is a major issue limiting the application of geostationary satellite observation in the Alaska region. Finally, the angular FOV and scan rate (sample number per scan) can be modified in the simulator to match future instrument design configuration.

b. Passive atmospheric sounders on LEO satellites

The most common scan mechanism used for passive atmospheric sounder on an LEO platform are 1) conic scanning and 2) cross-track scanning. Figure 10 shows example footprints of conical and cross-track scanning instruments that were assumed to be on board a stratospheric balloon platform, located at 18.3 km and 40.6°N, 117.8°W. The detailed method on how to compute the ground projection of the FOV (i.e., the GIFOV) can be found from the study by Wang et al. (2013) and the corresponding software can be obtained from the GitHub repository at https://github.com/wanglikun1973/ATMS_CrIS_footprint_computation. In this
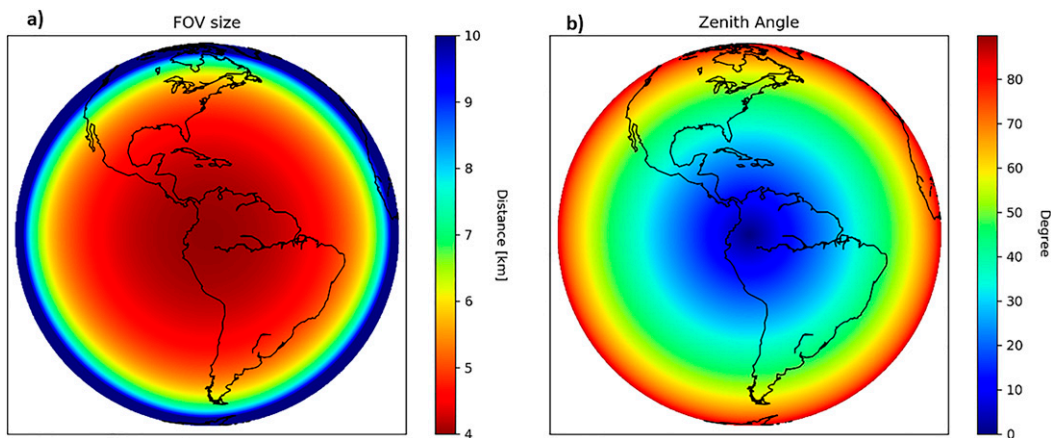

FIG. 9. (a) The pixel size resolution and (b) local zenith angle distribution for simulated sounder geometry dataset. The satellite subsatellite point is at 75°W on the equator.
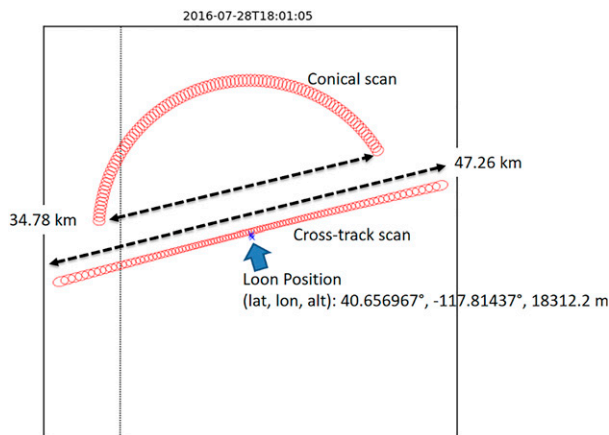
FIG. 10. Cross-track and conical scan simulations on a stratospheric balloon platform at the height of 18.3 km and at 40.6°N and 117.8°W.

simulation, each scan is composed of 96 FOVs with an FOV angle of 1.1°, which is defined as the angle subtended by a single detector element (infrared) or antenna main beam (microwave) on the axis of the optical system. The scan angle ranges from ±52.75° with a step angle of 1.1°. Conically scanning sounders such as the Special Sensor Microwave Imager (SSM/I) and the TRMM Microwave Imager (TMI), use a constant-angle rotary-scanning mechanism at a fixed angle of incidence while the platform travels forward. As a result (shown in Fig. 11), the satellite view zenith angle and GIFOV size are constant. However, conically scanning swath widths are usually less than the cross-track scanning swath widths. On the other hand, cross-track scanning radiometer, such as the Advanced Microwave Sounding Unit (ATMS) on the JPSS satellites, rotates perpendicular to the platform direction of travel, resulting in varying GIFOV size and view zenith angles. This results in degraded spatial resolution at wider scan angles.

Hyperspectral IR sounders, such as the Atmospheric Infrared Sounder (AIRS), the CrIS, and the Infrared Atmospheric Sounding Interferometer (IASI), generally use cross-track scanning. For an interferometer like CrIS or IASI, a detector array composed of several detectors increases data collection rate. For example, CrIS stepwise "stares" at Earth from −48.3° to +48.3° with a 3.3° step angle, collecting 30 fields of regards (FORs) of the Earth scenes. Each FOR contains a 3 × 3 set of observations made by 0.963° circular detectors separated by 1.1° (see Fig. 3 of Han et al. 2013), which corresponds to nine 14-km circular GIFOVs in the nadir FOR. This type of configuration as well as the other types of configurations described by Wang et al. (2016a) is supported by the simulator package. Shown in Fig. 12 is an example of simulated footprints of a 6 × 6 detector array with a nadir FOV size of 7.0 km projected on the Earth surface. As a step-scan Fourier transform spectrometer, the radiation from Earth and atmosphere is reflected into the instrument by a 45° mounted scan mirror rotating along two axes. Consequently, the GIFOVs of the 6 × 6 detectors rotate with increasing scan angles.

For validation purposes, the instrument simulator is used to simulate the orbit shown in Fig. 4a. Specifically, the following datasets are used as input, 1) static CrIS geometry calibration parameters that can be found from in the CrIS Sensor Data Records ATBD (Guenther 2011; Wang et al. 2017), 2) static CrIS scan parameters (e.g., FOV size and FOV number, scan speed, step angle and range), 3) dynamic satellite attitude angles from spacecraft diary data (such as pitch, roll, and yaw angles), and 4) dynamic satellite position and velocity vectors predicted from the platform simulator. The outputs are the CrIS geometry datasets that have the same content as the real data, including latitude and longitude, satellite view zenith and azimuths angles, and solar zenith angle and azimuth angles for each pixel. Figure 13 gives the location error in term of GIFOV in percent between the real dataset and those computed from the instrument simulator for all the pixels (a total of 220 320 measurements). The figure clearly shows that
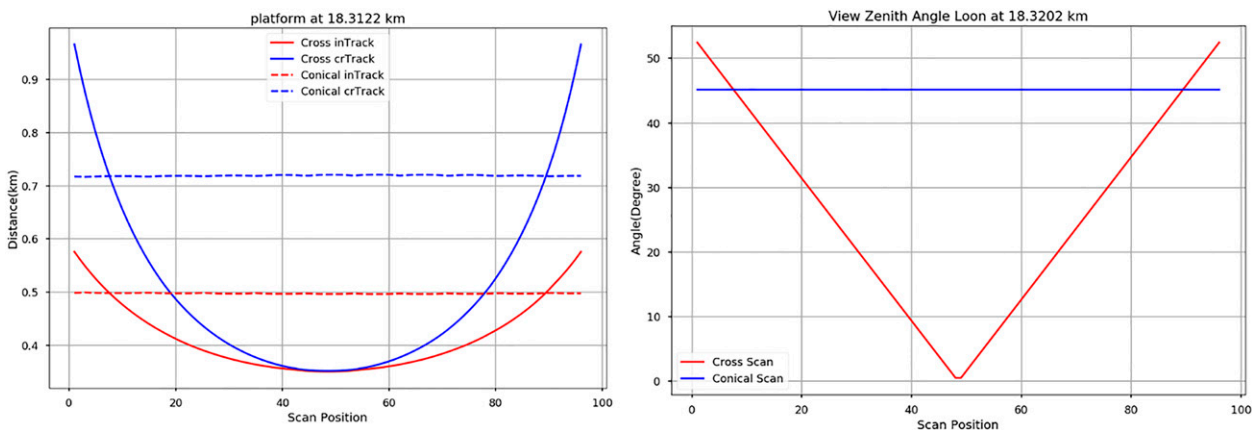

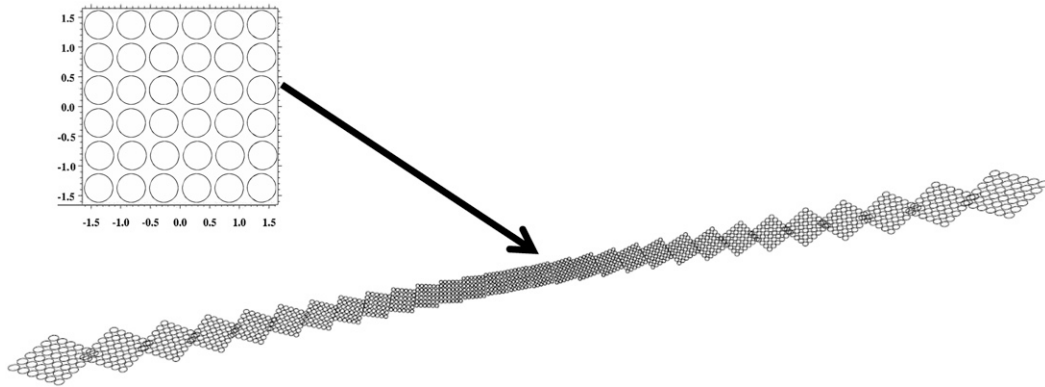FIG. 11. GIFOV dimensions along and cross track and view zenith angle for scan patterns shown in Fig. 10.

FIG. 12. An example of simulated footprints of a 6 × 6 detector array with an FOV size of 7.0 km projected on the Earth surface for CrIS-like hyperspectral IR sounders. The axis in the upper-right expanded plot is the detector size angle (°).

the location errors from the instrument simulator are less than 12% of the GIFOV (14 km corresponding to the CrIS FOV size of 0.963°). It should be noted that the CrIS GIFOV is a circle at nadir and gradually enlarges and becomes ellipsoidal as the scan angle increases. So that at the end of scan, the 14.0-km circle at nadir becomes an ellipse with major and minor axes of 43.6 and 23.2 km (see Fig. 12). As a result, the location errors are subpixel in size and negligible for OSSE studies.

c. Radio occultation simulator

RO relies on radio transmissions from the GPS satellites, or more generally from GNSS satellites in medium-Earth orbits that are monitored by a receiving platform, usually an LEO satellite (e.g., Constellation Observing System for Meteorology, Ionosphere, and Climate 2) but possibly in the future a stratosphere balloon. The signal passes through the atmosphere and gets refracted along the way. The magnitude of the refraction depends on the density and hence on the temperature and water vapor profiles in the atmosphere. The relative position between the GNSS satellite transmitter and the RO receivers on LEO orbit satellites or stratosphere balloons changes over time, allowing for a vertical scanning of successive layers of the atmosphere. Therefore, the occurrence of the RO observations depends on relative geometry between the GNSS transmitters and receivers. The goal of the RO observation geometry simulator is to compute the slant path between transmitter and receiver. The atmospheric profile can then be interpolated along the slant path, which is then converted into the RO excess phase, bending angle, or refractivity profile through an RO forward operator (e.g., Cucurull et al. 2007).

Figure 14 illustrates the geometry between the transmitters on the GNSS satellites (blue dots) and the receivers either on
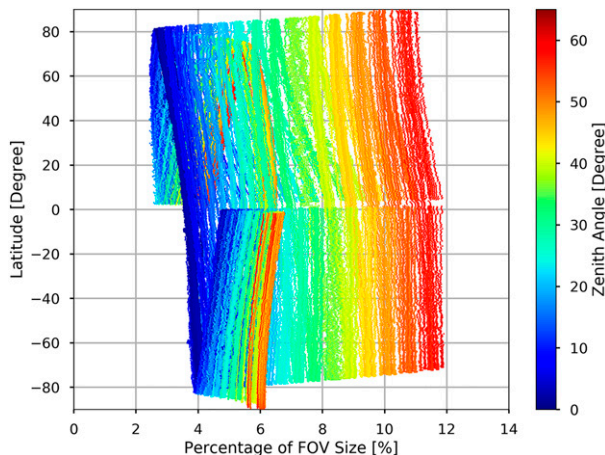

FIG. 13. The difference of measurement locations in term of the percentage of the FOV size between the real dataset and those predicted from the instrument simulator (a total of 220 320 measurements) for the orbit in Fig. 4. The color indicates the zenith angles.
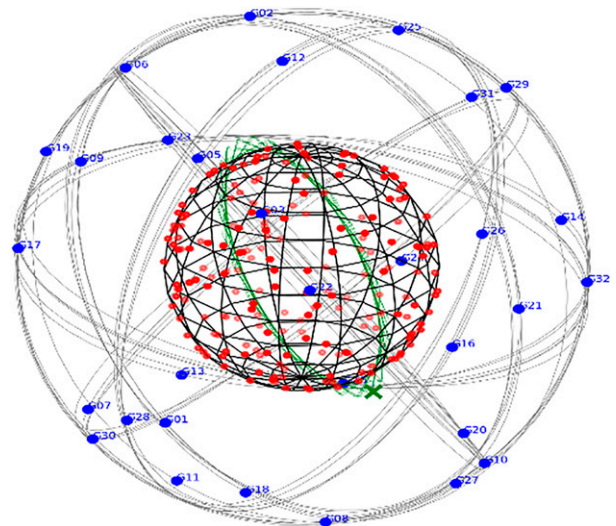

FIG. 14. The geometry between GPS transmitters on GPS satellites (blue dots) and receivers either on satellite (green lines) or stratosphere balloons (red dots). The figure is for illustration purposes and does not represent the exact scale of LEO and GPS satellite orbits.
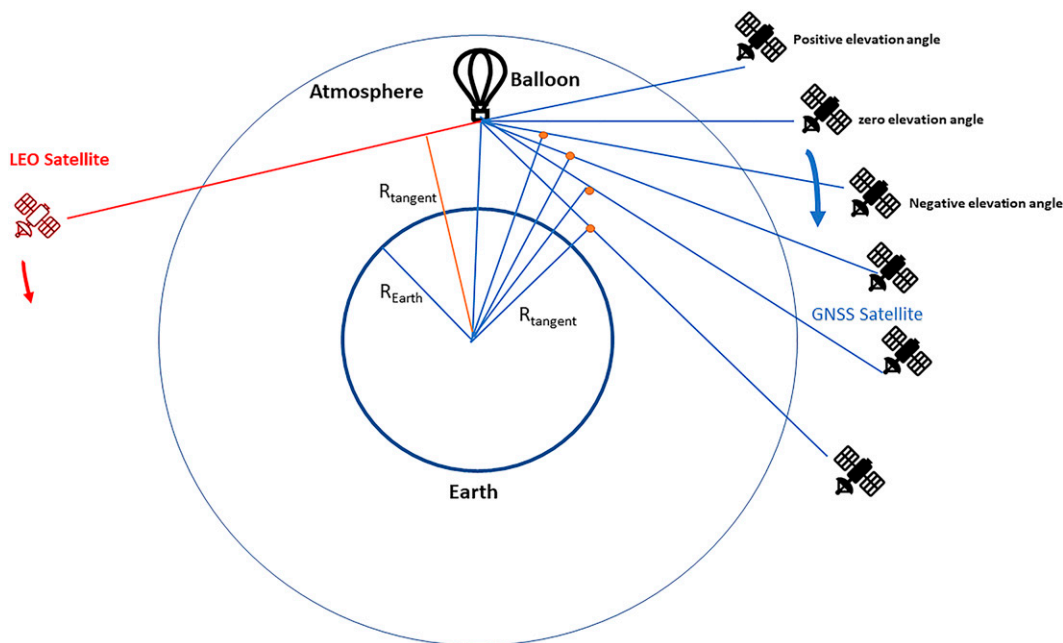
FIG. 15. Illustration of space- and balloonborne RO instruments.

LEO satellites (green lines) or stratosphere balloons (red dots) at a specific moment. The LEO satellites are typically 400–800 km above the surface of Earth, whereas the GNSS satellite are commonly at ∼20 200 km in a 12-h orbit. The transmitter and receivers are simultaneously moving along their respective orbits or paths. In the above sections, an orbit simulator to compute the LEO satellite position and a trajectory model to calculate the stratospheric balloon trajectory were developed. Instead of an orbit simulator for the GNSS satellites we obtain the exact position of the GNSS satellites from the International GNSS Service (IGS). The IGS maintains a high precision and accuracy catalog of GNSS satellite ephemerides (see the link http://www.igs.org/products). These data include the GNSS positions every 15 min with 3–5-cm accuracy (available from https://cddis.nasa.gov/). Figure 15 illustrates two types of the RO instruments: 1) the spaceborne RO where the GNSS signals are tracked by receivers outside the Earth atmosphere (e.g., Haase et al. 2014) and 2) the balloonborne RO where signals are received within the atmosphere.

Figure 16 is a flowchart that shows the procedures to compute the RO slant path. The following steps are taken, including 1) converting the GNSS receivers' platform position from (longitude, latitude, and altitude) into (x, y, z) in the ECEF coordinate and interpolating them to high temporal resolution (e.g., 0.1 s); 2) acquiring the GNSS satellite orbit products from NASA website (https://cddis.nasa.gov/) and also interpolating them to high temporal resolution; 3) computing the line of sight (LOS) vector that directly connects the GNSS receivers to the transmitters; 4) calculating the elevation angle, which is the angle viewing the GNSS satellite from the receiver's platform; 5) computing the straight-line tangent altitude (SLTA), which is the distance of the above the LOS vector to the surface of Earth (the difference between R_{tangent} and R_{Earth} in Fig. 15); 6) saving the cases where RO can occur by comparing to the preset elevation angle thresholds; and 7) outputting the time and location of GNSS RO slant path including longitude, latitude, and altitude. Though the GNSS signals from the GNSS satellites are broadcasting from all direction, only those falling within the GNSS receiver antenna can be processed to produce RO observations. This is determined by the GNSS receiver antenna pattern relative to the platform as well as the platform orientation. Therefore, for each GNSS signal, the simulator checks the azimuth angles to determine if they can reach the GNSS receiver.

Using the above algorithm, we predicted the RO occurrence locations for the GNSS Receiver for Atmospheric Sounding (GRAS) on board *MetOp-B* on 2 October 2018, which are compared with the real data and shown in Fig. 17. Note that the real RO locations stretch out horizontally in Fig. 17 because the locations of vertical bending angle profile are all shown.

Overall, the predicted RO positions agree well with the real data, though more ROs (697) are predicted than the real data (611). This is because the prediction algorithm assumes ideal condition while, the RO occurrence is impacted by the status and health of the GNSS transmitters, the GNSS receivers, and the on-orbit and ground processing. Therefore, the number of the GNSS ROs should be adjusted during OSSE experiments.

Zuffada et al. (1999) noted that, when the receiver is within the atmosphere (such as airborne or balloon-based GNSS RO), it is possible to measure both positive and negative elevation rays (as shown in Fig. 15). Specifically, for every
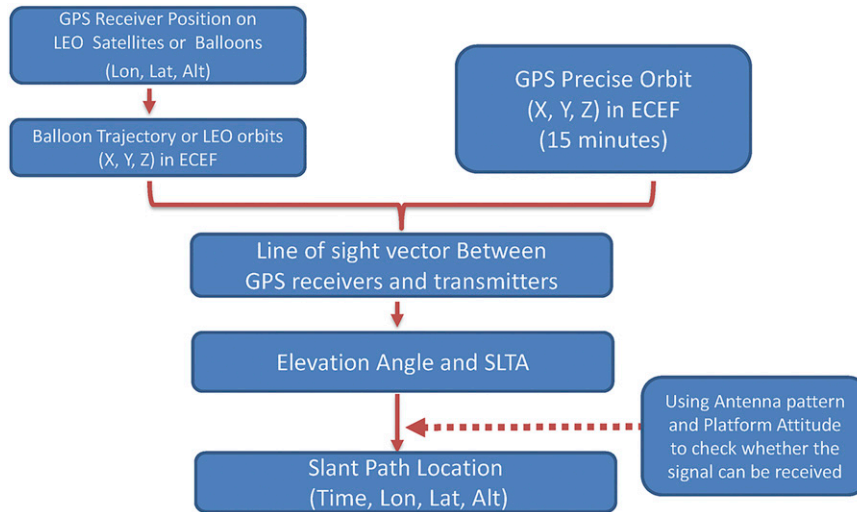
FIG. 16. Flowchart to compute balloon-based or LEO satellite-based GPS radio occultation slant path.

negative elevation ray with bending angle α_N, there is a corresponding positive elevation value α_P with the same impact parameter. The impact parameter a defines the radius of closest approach the ray path would have in the absence of bending. Mathematically, it is the product of the refractive index n, the radius of the ray path r, and the sine of the angle φ between the local radius vector and the tangent to the ray path (Healy et al. 2002). By assuming spherical symmetry, subtracting the positive elevation bending angle from the negative gives $\alpha'(a)$, the "partial bending angle" which is ray bending that occurs along the section of path below the receiver. Healy et al. (2002) proposed an approach using an Abel transform to estimate the atmospheric refractive index profile along the partial bending angle profiles. Figure 18 presents the comparison of the extended horizontal distance of LEO satellite-based (blue) and balloon-based (red) GNSS RO slant paths. From LEO, satellite-based bending angle profiles can extend from the near the surface to the top of the atmosphere. In addition, since LEO-based satellites move

outside the atmosphere, LEO-based receivers can "scan" the atmosphere as they orbit Earth. As a result, their horizontal distance slant paths are limited to around 80–100 km. By contrast, balloon-based RO can only extend vertically from the balloon platform to the surface; thus, providing no information content above the balloon. Furthermore, the GNSS receivers inside the atmosphere almost stand still compared to the GNSS satellites. Thus, scanning the atmosphere below the platform are achieved by viewing the slowly moving GNSS satellites, resulting in a relatively large horizontal distance of ~500 km. In addition, the RO forward operator for the balloon-based RO observations needs to be developed to compute the partial bending angle, which is different from the satellite-based RO forward operator in the CGOP package. All these differences need to be considered during the
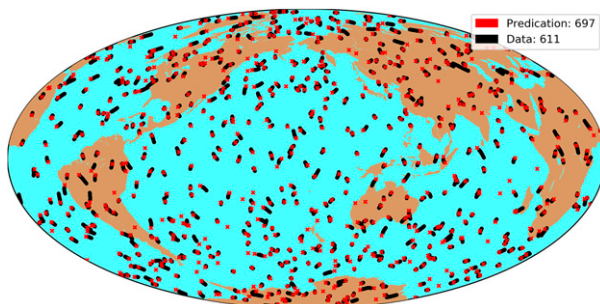

FIG. 17. Predicted (red) and real (black) RO locations for GRAS on *MetOp-B* on 2 Oct 2018. A total of 697 RO observations were predicted from the simulator, which are compared to 611 observations identified from the real data.
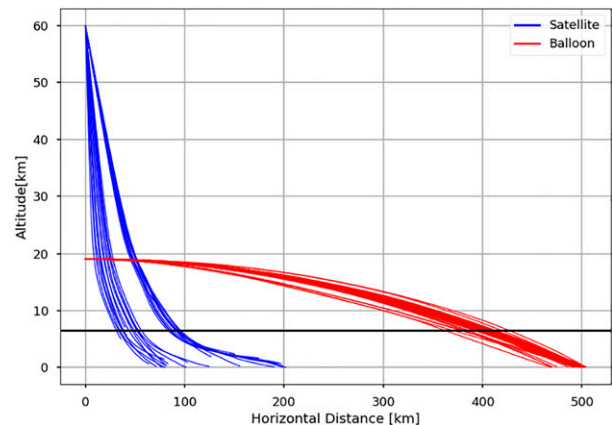

FIG. 18. Comparison of extended horizontal distance of LEO satellite-based (blue) and balloon-based (red) RO slant path. The altitude of the balloon is 19.0 km. The black line indicates the altitude of 7.0 km.
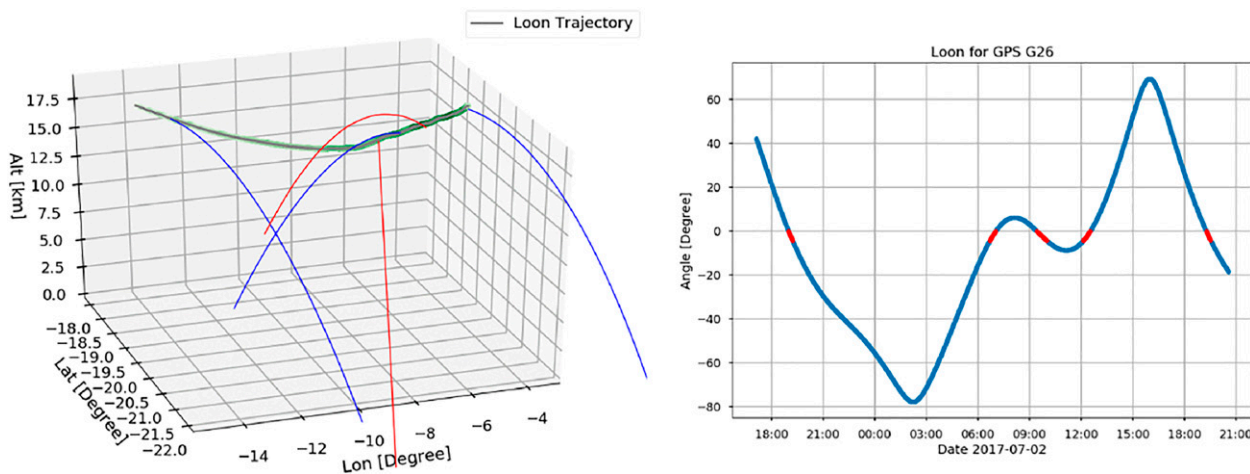
FIG. 19. An example of (left) the simulated balloon-based RO slant path in the 3D space and (right) their corresponding evaluation angles time series from the balloon to the GPS satellite G26. The green line indicates the Loon trajectory, while the rising and setting slant paths are indicated by the red and blue lines in the left panel.

OSSEs. Shown in Fig. 19 is an example of simulated balloon-based GNSS RO slant path in the 3D space and their corresponding elevation angle time series from the balloon to the GNSS satellite G26, where the balloon moves along its trajectory path at the altitude around 19.5 km (green line). In the figure, there are a total of five GNSS RO events, including three setting cases and two rising events.

4. Summary

The CGOP package developed at NOAA and JCSDA is used for OSSE studies to quantitatively evaluate the impacts of emerging observing system or new instruments on NOAA NWP systems. For any OSSE experiments, the first step is to simulate observations from the natural run. Hence the timing and locations of individual observations as well as the observing geometry is needed to extract the atmospheric and surface variables from the nature run, which are then input to the observation forward operator (e.g., radiative transfer model or RO forward operator). To address the challenge for newly proposed systems whose instruments are not yet built and platforms are not yet deployed, an orbit and near-space simulator to compute these parameters based on the specific hosting platform and onboard instrument characteristics has been recently developed under the GCOP framework. The software includes following parts.

1) The satellite orbit simulator can simulate the flying path of a satellite on a LEO, geostationary, and Tundra orbit once the orbit parameters are given. The simulator can output the satellite position and velocity vector at any moment, which can be further converted into longitude and latitude at nadir and satellite altitude. The validation for an existing satellite indicates that the simulator performs well and the errors for nadir locations are less than 0.6 km over one orbit.

2) A simple trajectory model for a superpressure stratospheric balloon platform is developed using G5NR wind fields. The balloon horizontally moves with winds and vertically stays on constant-density (isopycnic) surfaces. A qualitative assessment of computed and real balloon trajectories indicates that this simple trajectory model is sufficient to evaluate impacts of future instruments hosted on a balloon platform.

3) A module to account for platform orientation is also developed, which can be combined with the computed platform orbit (or trajectory) once the orientation angles (pitch, roll, and yaw) are available.

4) The instrument geometry simulator can simulate the observing geometry of passive atmospheric sounders on any platform. The calculated geometry parameters include time varying location (latitude and longitude), scan geometry (satellite zenith and azimuth angles), GIFOV shapes, and solar zenith and azimuth angles (if needed) for either cross-track or conical scanning mechanisms. Validation results for CrIS show that the simulator location errors are controlled at a subpixel level.

5) The radio occultation simulator determines the geometry of the GNSS transmitters and receivers either on satellites or stratospheric balloons and thus determines the slant path of the RO observations in the atmosphere. The comparison of predicted the GNSS RO occurrence against GRAS on board *MetOp-B* indicates that the prediction results are reasonable.

As a final note, we point out that, this simulator is purely for OSSE studies for evaluating the impacts for newly proposed instruments and platform; thus, it cannot replace existing ground processing software for satellite observations. In addition, the RO forward operator on the balloon platform is not available in the current CGOP package and needs to be developed in the future.

REFERENCES

Baker, N., 2011: Joint Polar Satellite System (JPPS) VIIRS geolocation. NOAA Algorithm Theoretical Basis Doc., 174 pp., https://www.star.nesdis.noaa.gov/jpss/documents/ATBD/D0001-M01-S01-004_JPSS_ATBD_VIIRS-Geolocation_A.pdf.

Barron, E. G., G. H. Kaplan, J. Bangert, J. L. Bartlett, W. Puatua, W. Harris, and P. Barrett, 2011: Naval Observatory Vector Astrometry Software (NOVAS) version 3.1. *Bull. Amer. Astron. Soc.*, **43**, 344.14.

Bingham, G. E., and Coauthors, 2006: Geosynchronous Imaging Fourier Transform Spectrometer (GIFTS) Engineering Demonstration Unit (EDU) overview and performance summary. *Proc. SPIE*, **6405**, 64050F, https://doi.org/10.1117/12.696861.

Boukabara, S.-A., and Coauthors, 2016: Community Global Observing System Simulation Experiment (OSSE) Package (CGOP): Description and usage. *J. Atmos. Oceanic Technol.*, **33**, 1759–1777, https://doi.org/10.1175/JTECH-D-16-0012.1.

——, and Coauthors, 2018a: Community Global Observing System Simulation Experiment (OSSE) Package (CGOP): Perfect observations simulation validation. *J. Atmos. Oceanic Technol.*, **35**, 207–226, https://doi.org/10.1175/JTECH-D-17-0077.1.

——, and Coauthors, 2018b: Community Global Observing System Simulation Experiment (OSSE) Package (CGOP): Assessment and validation of the OSSE system using an OSSE–OSE intercomparison of summary assessment metrics. *J. Atmos. Oceanic Technol.*, **35**, 2061–2078, https://doi.org/10.1175/JTECH-D-18-0061.1.

Candido, S., 2020: Loon stratospheric sensor data. Zenodo, accessed 23 April 2020, https://doi.org/10.5281/zenodo.3763022.

Casey, S., R. Atlas, R. N. Hoffman, L. Cucurull, and A. C. Kren, 2018: Geostationary Hyperspectral Sounder (Geo-HSS) constellation: A global OSSE assessment. *22nd Conf. on Integrated Observing and Assimilation Systems for the Atmosphere, Oceans, and Land Surface*, Austin, TX, Amer. Meteor. Soc., 4.2, https://ams.confex.com/ams/98Annual/webprogram/Paper333995.html.

Cucurull, L., J. C. Derber, R. Treadon, and R. J. Purser, 2007: Assimilation of global positioning system radio occultation observations into NCEP's Global Data Assimilation System. *Mon. Wea. Rev.*, **135**, 3174–3193, https://doi.org/10.1175/MWR3461.1.

de la Cámara, A., C. R. Mechoso, K. Ide, R. Walterscheid, and G. Schubert, 2010: Polar night vortex breakdown and large-scale stirring in the southern stratosphere. *Climate Dyn.*, **35**, 965–975, https://doi.org/10.1007/s00382-009-0632-6.

Friedrich, L. S., A. J. McDonald, G. E. Bodeker, K. E. Cooper, J. Lewis, and A. J. Paterson, 2017: A comparison of Loon balloon observations and stratospheric reanalysis products. *Atmos. Chem. Phys.*, **17**, 855–866, https://doi.org/10.5194/acp-17-855-2017.

Guenther, B., 2011: Joint Polar Satellite System (JPSS) Cross Track Infrared Sounder (CrIS) Sensor Data Records (SDR). NASA Algorithm Theoretical Basis Doc., 66 pp., https://www.jpss.noaa.gov/sciencedocuments/sciencedocs/2017-06/474-00071_OAD-CrIS-SDR_F.pdf.

Haase, J. S., B. J. Murphy, P. Muradyan, F. G. Nievinski, K. M. Larson, J. L. Garrison, and K.-N. Wang, 2014: First results from an airborne GPS radio occultation system for atmospheric profiling. *Geophys. Res. Lett.*, **41**, 1759–1765, https://doi.org/10.1002/2013GL058681.

Han, Y., and Coauthors, 2013: Suomi NPP CrIS measurements, sensor data record algorithm, calibration and validation activities, and record data quality. *J. Geophys. Res. Atmos.*, **118**, 12 734–12 748, https://doi:10.1002/2013JD020344.

Healy, S. B., J. Haase, and O. Lesne, 2002: Abel transform inversion of radio occultation measurements made with a receiver inside the Earth's atmosphere. *Ann. Geophys.*, **20**, 1253–1256, https://doi.org/10.5194/angeo-20-1253-2002.

Hertzog, A., and Coauthors, 2007: Stratéole/Vorcore—Long-duration, superpressure balloons to study the Antarctic lower stratosphere during the 2005 winter. *J. Atmos. Oceanic Technol.*, **24**, 2048–2061, https://doi.org/10.1175/2007JTECHA948.1.

Hoffman, R. N., and R. Atlas, 2016: Future observing system simulation experiments. *Bull. Amer. Meteor. Soc.*, **97**, 1601–1616, https://doi.org/10.1175/BAMS-D-15-00200.1.

Levanon, N., R. A. Oehlkers, S. D. Ellington, W. J. Massman, and V. E. Suomi, 1974: On the behavior of superpressure balloons at 150 mb. *J. Appl. Meteor.*, **13**, 494–504, https://doi.org/10.1175/1520-0450(1974)013<0494:OTBOSB>2.0.CO;2.

Li, Z., and Coauthors, 2018: Value-added impact of geostationary hyperspectral infrared sounders on local severe storm forecasts—Via a quick regional OSSE. *Adv. Atmos. Sci.*, **35**, 1217–1230, https://doi.org/10.1007/s00376-018-8036-3.

——, T. J. Schmit, J. Li, M. M. Gunshor, and F. W. Nagle, 2021: Understanding the imaging capability of Tundra orbits compared to other orbits. *IEEE Trans. Geosci. Remote Sens.*, **59**, 8944–8956, https://doi.org/10.1109/TGRS.2021.3051527.

NOAA, 2018: GOES-R series data book. NASA Doc. CDRL PM-14, 240 pp., https://www.goes-r.gov/downloads/resources/documents/GOES-RSeriesDataBook.pdf.

Putman, W., A. M. da Silva, L. E. Ott, and A. Darmenov, 2014: Model configuration for the 7-km GEOS-5 nature run, Ganymed release (non-hydrostatic 7 km global mesoscale simulation). NASA GMAO Office Note 5, version 1.0, 18 pp., http://gmao.gsfc.nasa.gov/pubs/docs/Putman727.pdf.

Riddle, E. E., P. B. Voss, A. Stohl, D. Holcomb, D. Maczka, K. Washburn, and R. W. Talbot, 2006: Trajectory model validation using newly developed altitude-controlled balloons during the International Consortium for Atmospheric Research on Transport and Transformations 2004 campaign. *J. Geophys. Res.*, **111**, D23S57, https://doi.org/10.1029/2006JD007456.

Rößler, T., O. Stein, Y. Heng, P. Baumeister, and L. Hoffmann, 2018: Trajectory errors of different numerical integration schemes diagnosed with the MPTRAC advection module driven by ECMWF operational analyses. *Geosci. Model Dev.*, **11**, 575–592, https://doi.org/10.5194/gmd-11-575-2018.

Schmit, T. J., J. Li, S. A. Ackerman, and J. J. Gurka, 2009: High-spectral- and high-temporal-resolution infrared measurements from geostationary orbit. *J. Atmos. Oceanic Technol.*, **26**, 2273–2292, https://doi.org/10.1175/2009JTECHA1248.1.

Stunder, B. J. B., 1996: An assessment of the quality of forecast trajectories. *J. Appl. Meteor.*, **35**, 1319–1331, https://doi.org/10.1175/1520-0450(1996)035<1319:AAOTQO>2.0.CO;2.

Trishchenko, A. P., L. Garand, L. D. Trichtchenko, and L. V. Nikitina, 2016: Multiple-apogee highly elliptical orbits for continuous meteorological imaging of polar regions: Challenging the classical 12-h Molniya orbit concept. *Bull. Amer. Meteor. Soc.*, **97**, 19–24, https://doi.org/10.1175/BAMS-D-14-00251.1.

Vallado, D. A., P. Crawford, R. Hujsak, and T. S. Kelso, 2006: Revisiting Spacetrack Report #3: Rev 1. *Astrodynamics Specialist Conf. and Exhibit*, Keystone, CO, AIAA/AAS, AIAA 2006-6753, https://doi.org/10.2514/6.2006-6753.

Wang, L., and Coauthors, 2013: Geolocation assessment for CrIS sensor data records. *J. Geophys. Res. Atmos.*, **118**, 12 690–12 704, https://doi.org/10.1002/2013JD020376.

——, Y. Chen, and Y. Han, 2016a: Impacts of field of view configuration of Cross-Track Infrared Sounder on clear sky observations. *Appl. Opt.*, **55**, 7113–7119, https://doi.org/10.1364/AO.55.007113.

——, D. Tremblay, B. Zhang, and Y. Han, 2016b: Fast and accurate collocation of the Visible Infrared Imaging Radiometer Suite measurements with Cross-Track Infrared Sounder. *Remote Sens.*, **8**, 76, https://doi.org/10.3390/rs8010076.

——, B. Zhang, D. Tremblay, and Y. Han, 2017: Improved scheme for Cross-Track Infrared Sounder geolocation assessment and optimization. *J. Geophys. Res. Atmos.*, **122**, 519–536, https://doi.org/10.1002/2016JD025812.

Wang, P., Z. Li, J. Li, and T. J. Schmit, 2021: Added value of GEO-hyperspectral infrared radiances for local severe storm forecasts using hybrid OSSE method. *Adv. Atmos. Sci.*, **38**, 1315–1333, https://doi.org/10.1007/s00376-021-0443-1.

Zuffada, C., G. A. Hajj, and E. R. Kursiniski, 1999: A novel approach to atmospheric profiling with a mountain-based or airborne GPS receiver. *J. Geophys. Res.*, **104**, 24 435–24 447, https://doi.org/10.1029/1999JD900766.